

Multilayered MXenes for future two-dimensional nonvolatile magnetic memories

P. Kumar,¹ Y. Miura,^{1,2} Y. Kotani,³ A. Sumiyoshiya,³ T. Nakamura,^{3,4} Gaurav K. Shukla,¹ and S. Isogami^{1}*

¹ Research Center for Magnetic and Spintronic Materials,
National Institute for Materials Science (NIMS).
Sengen 1-2-1, Tsukuba, Ibaraki, 305-0047, JAPAN.

² Faculty of Electrical Engineering and Electronics,
Kyoto Institute of Technology.
Hashikami-cho, Matsugasaki, Sakyo-ku, Kyoto, 606-8585, JAPAN

³ Photon Science Innovation Center (PhoSIC),
NanoTerasu.
Aoba 468-1, Aramaki-Aza, Aoba, Sendai, 980-8572, JAPAN.

⁴ International Center for Synchrotron Radiation Innovation Smart (SRIS),
Tohoku University.
Aoba 468-1, Aramaki-Aza, Aoba, Sendai, 980-8572, JAPAN.

KEYWORDS

Two-dimensional MXene, Spin transport, Current-induced magnetization switching, XMCD, MRAM

ABSTRACT

MXenes have attracted considerable attention in recent years due to their two-dimensional (2D) layered structure with various functionalities similar to the existing graphene and transition metal dichalcogenides. Aiming to open a new application field for MXenes in the realm of electronic devices such as ultrahigh-integrated magnetic memory, we have developed a spin-orbit torque (SOT) bilayer structure consisting of bare MXene of Cr_2N : substrate// $\text{Cr}_2\text{N}/[\text{Co}/\text{Pt}]_3/\text{MgO}$ using magnetron sputtering technique. We demonstrate the field-free current-induced magnetization switching (CIMS) in the Hall-cross configuration with the critical current density of $\sim 30 \text{ MA}/\text{cm}^2$. An attempt to replace the Cr_2N layer by the Pt layer leads to the absence of field-free CIMS. As the SOT efficiency increases with increasing the Cr_2N thickness, the first-principles calculation predicts the pronounced orbital-Hall conductivity in the out-of-plane component, compared to the spin-Hall conductivity in the Cr_2N . X-ray magnetic circular dichroism reveals the out-of-plane uncompensated magnetic moment of Cr ($m_{\text{Cr}}^{\text{U.C.}}$) in the Cr_2N layer at the interface, by contacting with Co in the $[\text{Co}/\text{Pt}]_3$ ferromagnetic layer. The interfacial spin-filtering-like effect against the out-of-plane polarized spin owing to the $m_{\text{Cr}}^{\text{U.C.}}$ might be a possible cause for the field-free CIMS. These results show a significant milestone in the advanced 2D-spintronics, promising low-power and ultrahigh-integration.

Introduction

The importance of semiconductor devices is rapidly increasing due to the development of a modern society in which humans are connected to all kinds of applications via the Internet. To realize efficient devices for the society, two-dimensional (2D) materials such as the single-layer graphene and the transition metal dichalcogenides (TMDC) have attracted significant attention in the view of their various functionalities.^[1-9] On the other hand, a transition metal carbide Ti_3C_2 with atomic layered structures was first discovered in 2011,^[10] which has opened a new class of 2D materials. It is called MXene and known as a post graphene and TMDC.^[11] The chemical formula is $M_{n+1}X_nT_x$, where the site M represents the transition metals such as Ti and Cr, X represents the $2p$ light elements of C or N, and T represents the surface terminations such as O and Cl on the outer M layer. The n varying from 1 to 4 corresponds to the number of the simplest M - X - M bonding trilayer-unit of M_2X , while x is variable. The physical and chemical properties can be tailored by n , as well as various combinations of M , X , and T .^[12] These characteristics are related to the significant electronegativity for the $2p$ light elements X , which allows for the strong orbital hybridization with the M elements.^[13] Thus, the MXenes are widely considered to have immense potential as a key material for many device applications. In the past decade, the MXene has contributed to the fields of, e.g., biomedical,^[14] mechanical,^[15] optoelectronics,^[16] and energy storage.^[17] These pioneering works inspire our interest in finding a more remarkable potential of MXene. In this study, we aim to develop another new application field of MXene historically by expanding into the field of 2D spintronics,^[18,19] that has been unfamiliar with MXene and elucidating its superiority. Furthermore, we look deeply into the MXene-specific spin transport phenomena beyond the charge transport.

In the spintronics research, manipulation of magnetic moment via spin degree of freedom has attracted considerable attention in terms of electronic devices with low power consumption, because the spin current, a flow of spin angular momentum without electron charge, does not consume power in principle.^[20] In particular, to store the enormous amount of data associated with the widespread of internet and mobile applications, a nonvolatile spin-orbit torque magnetic random access memory (SOT-MRAM) has been extensively studied as one of the storage devices taking advantages of the spin current.^[21] Although three types of SOT-MRAMs with the magnetization directions of the recording layer in x , y and z have been proposed,^[22] the so-called Type-Z with a perpendicularly oriented magnetization (in z direction) has been identified as a promising geometry for further high integration and low power of the MRAM packages. However, the Type-Z needs an in-plane bias magnetic field for writing by the conventional in-plane current-induced SOT, originating from the spin current in the conventional heavy metals such as Ta, Pt and W. This has been an issue for achieving the miniaturization of cell size and high integrated SOT-MRAMs, leading to a recent challenge for field-free current-induced magnetization switching (CIMS) by SOT, and many approaches have been demonstrated to date:^[23] the compositional and/or geometrical gradient in the multilayers;^[24,25] the interfacial engineering by nonmagnetic layers;^[26,27] the exchange coupling between antiferromagnet/ferromagnet bilayers;^[28,29] the crystal symmetry of noncollinear antiferromagnet and TMDC;^[30-37] and the complex circuit architecture with combined SOT and spin-transfer-torque.^[38,39] These are based on the concepts of how the out-of-plane SOT component can be superimposed on the conventional in-plane SOT. Contrary to the artificial structure and materials mentioned above for out-of-plane SOT, we focus on the sputter-deposited bare MXene (M_2X) film with the simplest ($n = 1$) trilayer structure without T layer, which has a hexagonal structure similar to the existing TMDC of WTe_2 .^[33-37] Although there are many candidates for the M site such as Ti, V, W, Mo, and Cr, we

employ the Cr₂N as a bare MXene in terms of the phase stability and high conductivity as in the case of conventional transition-metal nitrides.^[40,41] The points to be highlighted for the MXene-based SOT-device could be a pronounced orbital current generation due to the light elements in MXene in addition to the spin current, promising a unique CIMS.

In Fig. 1, we show the possible concept of the field-free CIMS in the MXene-based SOT-device based on the findings in this study. Firstly, the orbital current in the Cr₂N layer could be expected originating from the orbital Hall effect (OHE), which dominates the entire SOT exerted at the ferromagnetic layer. Secondly, the nonmagnetic Cr layer, i.e., the top layer of Cr₂N MXene unit, adjacent to the ferromagnetic layer can polarize, resulting in an uncompensated magnetic moment of Cr ($m_{\text{Cr}}^{\text{U.C.}}$) with out-of-plane direction as depicted by thick arrows at the interface. This could be dominantly responsible for the superposition of the out-of-plane SOT component due to a spin-filtering-like mechanism at the interface.^[27,42] Namely, the spin converted from the orbital angular momentum with the same direction as the $m_{\text{Cr}}^{\text{U.C.}}$, can be transferred, while cannot for the spin with opposite direction. As a result, the field-free CIMS occurs, which might be the unique mechanism for the MXene-based SOT-devices, that cannot be identified for the TMDCs such as WTe₂,^[33,34] regardless of the similar 2D materials. Furthermore, the Cr₂N MXene film can be formed by sputtering technique with relatively low substrate temperature. These results led us to conclude that the MXene could be beneficial for SOT-MRAM in terms of device miniaturization owing to the field-free CIMS, and the robust bottom-up and stable productivity.

Results and discussion

The unit cell of Cr₂N MXene shows a hexagonal structure with the space group of $P6_3/mmc$ as shown in Fig. 2(a1), and the lattice constants are $a = b = 0.48$ nm and $c = 0.45$ nm. The collinear antiferromagnetic structure is reported for the wide temperature range from 100 K to 500 K,^[43-47]

which was also predicted by our first-principles calculations as indicated by arrows on each Cr atom. The cross-sectional view and the plane view are shown together with their coordinates in Figs. 2(a2) and 2(a3), where the Cr atoms at the top layer are surrounded by the black circles to distinguish the bottom Cr layer. Both top and bottom Cr layers show close-packed structure and the N atoms are present at the octahedral sites in between two Cr layers. Note that the present Cr₂N belongs to the family of bare MXene without the *T* sites, but the Cr-N-Cr trilayer unit is stacked bonded by N layer. Figure 2(b1) shows the out-of-plane X-ray diffraction (XRD) profiles for the pure Cr, CrN, and Cr₂N films with the thickness of ~20 nm on the *c*-plane oriented Al₂O₃ substrate. Each phase can be formed by different ratio of N₂ gas flow defined as $Q = N_2/(Ar + N_2)$ in the reactive sputtering deposition. For $Q = 0\%$, the pure Cr film was grown with the (110) texture. For $Q = 5\%$, the fringe oscillation was observed near the XRD peak at $2\theta/\omega \approx 40^\circ$ and 88° , suggesting the Cr₂N formation with hexagonal crystal structure and atomically flat surfaces. For $Q = 10\%$, the CrN, which is another phase of the Cr-N intermetallic compound with face-centered-cubic structure, was grown in (111) texture. Figure 2(b2) shows the substrate temperature (T_{sub}) dependence of out-of-plane XRD profiles for the Cr₂N film with the same thicknesses. Although the texture with (0001) orientation can be grown even at room temperature (RT), high atomic order was obtained at the T_{sub} ranging from 350 °C to 650 °C. Figure 2(c1) shows the high-resolution cross-sectional transmission microscopy (TEM) images of Cr₂N deposited at 650 °C. The bright balls in the enlarged image correspond to the Cr atoms, and the multi-stacking of the Cr₂N MXene unit is confirmed with atomically flat interfaces and an extremely high atomic ordering. The nano electron-beam diffraction patterns shown in Fig. 2(c2) shows the bright and dark spots originating from the fundamental lattice and the superlattice of the Cr₂N, respectively, which can be also confirmed in the out-of-plane XRD profiles in Fig. 2(b1). The content of Cr and N was evaluated to be 66.03 at.% and 33.97 at.%, respectively, via the energy dispersive spectroscopy, suggesting

the stoichiometric Cr₂N (see Fig. S1 in Supporting Information). These results show that the Cr₂N layer grown on the Al₂O₃ substrate could be a pseudo single crystal, which is close to the bulk single crystal of MXene. Figures 2(d) and 2(e) show the in-plane magnetic property (in x -direction) and the anomalous Hall measurement with the magnetic field along the out-of-plane (in z -direction) of the Cr₂N layer. The magnetization was negligible without hysteresis, which can be attributed to the antiferromagnetism of Cr₂N as predicted by the first-principles calculation.^[43-47]

To investigate the CIMS characteristics owing to the Cr₂N MXene, we prepared SOT-devices as depicted in Fig. 3(a): substrate//Cr₂N(5 nm)/[Co(0.35 nm)/Pt(0.3 nm)]₃/MgO(2 nm). The Co/Pt multilayer with three periods, which is described as [Co/Pt]₃, provides us with sufficient perpendicular magnetic anisotropy, resulting in the out-of-plane magnetization ($M_{\text{Co/Pt}}$) at the remanent state (see Fig. S2 in Supporting Information). Figure 3(b) exhibits the (0001) plane of Cr₂N supercell that is the same as in Fig. 2(a3), and a mirror symmetry can be seen with respect to the blue dashed line (m). In order to draw out the specific characteristics for the Cr₂N/ferromagnet system that cannot be explained by such mirror symmetry, we intentionally applied the charge current pulse parallel to this mirror axis (in x -direction), in which the out-of-plane SOT is observed to be vanished in the case of WTe₂/ferromagnet systems.^[33,34] The anomalous Hall resistance (R_{xy}) with the magnetic field sweep along the out-of-plane (H_z) and in-plane (H_x) directions are shown in Figs. 3(c1) and 3(c2), respectively, where the $M_{\text{Co/Pt}}$ is described by arrows. The R_{xy} amplitude for $\mu_0 H_z = 0$ was consistent with that for $\mu_0 H_x = 0$, suggesting the sufficient perpendicular magnetic anisotropy in the [Co/Pt]₃ layer so that the $M_{\text{Co/Pt}}$ points in z -direction at the magnetic remanent state. Figure 3(c3) shows the CIMS behaviors under the bias field of H_x , where the load current pulse duration is 10 ms. The change in the R_{xy} corresponding to the magnetization switching was remarkably sharp as observed in the conventional heavy-metal based SOT-device with Type-Y geometry,^[48] and the polarity of CIMS loop depending on the H_x was clockwise (CW) for $\mu_0 H_x =$

+29 mT and counter-clockwise (CCW) for $\mu_0 H_x = -18$ mT. It should be noted that the partial CIMS occurred at $\mu_0 H_x = 0$ (field free) as shown in Fig. 3(c4), and the effective critical current density flowing in the Cr₂N layer ($J_{\text{Cr}_2\text{N}}$) was ~ 30 MA/cm². Here, the value was given by eliminating the current shunting to the [Co/Pt]₃ layer based on the measured resistivity of both Cr₂N and [Co/Pt]₃ layers (see Fig. S3 in Supporting Information). Note that the $J_{\text{Cr}_2\text{N}}$ obtained are comparable to that of the Type-Y devices,^[48] which includes heavy metals with strong SOC and high SOT efficiency. The polarity of the field-free CIMS was CW, which was confirmed in the other 10~20 devices measured. The pulse duration in the demonstration is 10 ms, so that the observed results are in line with the view of thermally activated CIMS.^[49,50] The thermal stability factor Δ is given by,^[49]

$$J_c = J_0 \left(1 - \frac{1}{\Delta} \ln \left(\frac{t_p}{\tau_0} \right) \right), \quad (1)$$

where t_p and τ_0 represent the pulse duration and the inverse attempt frequency of 10^9 Hz, respectively. By fitting to the plots in Fig. 3(d) with $t_p = 1$ ms \sim 100 ms using the Eq. (1), we obtained the Δ value for the CIMS from down to up (up to down) as ~ 67 (~ 62), suggesting the high thermal stability promising the data retention for 10 years. The $J_{\text{Cr}_2\text{N}}-H_x$ diagram shown in Fig. 3(e) revealed that the $J_{\text{Cr}_2\text{N}}$ decreased with increasing H_x , and the field-free CIMS was achieved even at lower $T_{\text{sub}} = 350$ °C. In the production line of the CMOS transistor, in which the SOT-MRAMs are to be embedded, post-annealing has been performed at ~ 400 °C. Note that the Cr₂N based SOT-devices have enough heat endurance to show the stable CIMS, owing to the robustness of Cr₂N crystal structure against growth temperature [Fig. 2(b2)]. The ratio of field-free CIMS to the full CIMS was approximately 20% regardless of T_{sub} as shown in Fig. 3(f). These intermediate states were observed in the other devices as well we measured (see Fig. S4 in Supporting Information). Because the [Co/Pt]₃ ferromagnetic layer of Hall-cross device has large area with $10 \mu\text{m} \times 7 \mu\text{m}$, multiple domain structures would form when the CIMS occurs, resulting

in such an intermediate magnetic state.^[51] Therefore, it is speculated that microfabrication into nano-pillars or Hall-cross consisting of nano-wires would be one of the approaches to achieve the field-free and full CIMS.^[52,53] Nevertheless, the ratio can be enhanced by the 1-nm-thick Cr insertion (blue symbol), while slightly suppressed by the 1-nm-thick Pt insertion (green symbol), suggesting the relationship between the interfacial phenomena and the out-of-plane SOT component, as discussed in Figs. 5 and 6.

To assess the possible mechanism of the SOT, the effective efficiency (ξ_{eff}) was quantified for the samples with various Cr₂N thickness: substrate//Cr₂N(t_{Cr2N})/[Co(0.35 nm)/Pt(0.3 nm)]₃/MgO(2 nm). Figures 4(a1) and 4(a2) show the out-of-plane AHE and CIMS loops. The amplitude of R_{xy} reduced with increasing the current-shunting into the Cr₂N layer, so that we multiplied factors to expand the loops for visibility. It can be seen the amplitude in the AHE and that in the CIMS are comparable for each t_{Cr2N} , and the critical current density of J_{Cr2N} decreased with increasing t_{Cr2N} . The ξ_{eff} was estimated using the equation,^[54,55]

$$\xi_{\text{eff}} = \left(\frac{2e}{\hbar}\right) \left(\frac{M_s t_{\text{Co/Pt}} H_p}{J_{\text{Cr2N}}}\right), \quad (2)$$

where M_s and H_p represent the saturation magnetization of Co/Pt ferromagnetic layer and the domain wall depinning field that is defined as $H_c = H_p/\cos\theta$, respectively.^[54,55] Because the CIMS in the present Hall-cross structure occurs through the domain nucleation and propagation process, the H_p value is necessary to estimate for the ξ_{eff} as shown in Eq. (2). The H_p was determined by measuring the H_c as a function of the polar angle (θ) with respect to the film surface (see Fig. S5 in Supporting Information). Note that the current-shunting into the [Co/Pt]₃ layer was excluded from J_{Cr2N} by multiplying the ratio of sheet-resistance of Cr₂N layer to the entire sheet resistance. It was revealed that ξ_{eff} monotonically increased with increasing t_{Cr2N} as shown in the red symbols

of Fig. 4(c). To verify such thickness dependence, we examined the ξ_{eff} by another method, that is, second-harmonic SOT measurements. Figures 4(b1) and 4(b2) show the first-harmonic and the second-harmonic Hall resistance, respectively, for the sample with $t_{\text{Cr2N}} = 3.6$ nm. To distinguish the damping-like and field-like SOTs, and various magneto thermoelectric components,^[56] such as ordinary Nernst effect and anomalous Nernst effect, we conducted the data fitting using the following equation,^[56]

$$R_{xy}^{2\omega} = \frac{R_{\text{AHE}}}{2} \frac{H_{\text{DL}}}{|H_x| - H_{\text{k}}^{\text{eff}}} + R_{\text{PHE}} \frac{H_{\text{FL+Oe}}}{|H_x|} + R_{\text{TH}}, \quad (3)$$

at the high-field regime as shown in Fig. 4(b2). R_{AHE} , R_{PHE} , and R_{TH} are the amplitude of anomalous Hall resistance, the amplitude of planar-Hall resistance obtained by the magnetization rotation on the xy -plane, and the resistance originating from the magneto thermoelectric effect, respectively. $H_{\text{k}}^{\text{eff}}$ is the effective anisotropy field estimated using Eq. (S2) in the Supporting Information. H_{DL} and $H_{\text{FL+Oe}}$ are the damping-like SOT effective field and the superposition of field-like effective field and oersted field, respectively. Using $R_{\text{AHE(PHE)}} \approx 7.5 \Omega$ (0.1Ω) and $H_{\text{k}}^{\text{eff}} \approx 0.6$ T, we obtained $\mu_0 H_{\text{DL}} \approx 4.2$ mT and $\mu_0 H_{\text{FL+Oe}} \approx 0.30$ mT, resulting in $\xi_{\text{eff}} = \mu_0 H_{\text{DL}} / J_{\text{Cr2N}} \approx 0.66$ mT/MA cm^{-2} for $t_{\text{Cr2N}} = 3.6$ nm. Note that R_{TH} corresponding to the offset with respect to $R_{xy}^{2\omega} \approx 0$ at high-field (~ 2 T) [Fig. 4(b2)], suggesting that the magneto thermoelectric effect can be ruled out from the major origin for CIMS in the present $\text{Cr}_2\text{N}/[\text{Co}/\text{Pt}]_3$ system. These results demonstrate that ξ_{eff} dependence on t_{Cr2N} via second-harmonic measurements agreed with that via CIMS as shown in Fig. 4(c).

To explore the relationship between the SOT and the interface phenomena, we measured the element selective magnetic properties at the $\text{Cr}_2\text{N}/\text{ferromagnetic}$ interfaces by means of X-ray magnetic circular dichroism (XMCD) for three samples [Figs. 5(a1)-5(a2)]: (a1) the pure Co for

comparison; (a2) the Cr₂N/Co bilayer; and (a3) the Cr₂N/Pt bilayer. The XMCD signals are shown in Figs. 5(b)-5(d), and Table 1 summarizes the spin (m_{spin}) and orbital (m_{orb}) magnetic moment for Co, Cr, and N estimated using the Sum rule (see Fig. S6 in Supporting Information).^[57,58] The resultant values of pure Co ($m_{\text{spin}} \approx 1.83 \mu_{\text{B}}$; $m_{\text{orb}} \approx 0.17 \mu_{\text{B}}$) were consistent with the calculation results of $m_{\text{spin}} \approx 1.63 \mu_{\text{B}}$ and $m_{\text{orb}} \approx 0.1 \mu_{\text{B}}$,^[59] while those for the Cr₂N/Co ($m_{\text{spin}} \approx 0.99 \mu_{\text{B}}$; $m_{\text{orb}} \approx 0.073 \mu_{\text{B}}$) were smaller compared to the pure Co. On the other hand, Cr in the Cr₂N/Co was clearly polarized to be $m_{\text{spin}} \approx -0.063 \mu_{\text{B}}$ as shown in Fig. 5(c), which are close to the values for Cr₂O₃/Co systems reported.^[60] Conversely, the $m_{\text{spin(orb)}}$ of Cr in the Cr₂N/Pt was negligible. These results show the presence of $m_{\text{Cr}}^{\text{U.C.}}$ originating from the imbalance of antiferromagnetic structure of Cr₂N due to the adjacent Co layer as mentioned in Fig. 1. Regarding the N polarization, however, $m_{\text{spin(orb)}}$ was negligible as shown in Table 1 and Fig. 5(d), while the N in the Fe-N system shows the finite $m_{\text{spin(orb)}}$.^[61] These results confirm the atomic layered structure of Cr₂N, which is terminated by the Cr atomic layer at the Cr₂N/Co interface. To provide further insights into the $m_{\text{Cr}}^{\text{U.C.}}$, we measured the element-selective magnetic hysteresis loops along the H_z direction for the Co L_3 -edge and Cr L_3 -edge as shown in Fig. 5(e). Sharp magnetization switching of Co and Cr were evident at the same H_z , suggesting that the magnetic easy-axis aligns in the out-of-plane. And the switching directions were opposite each other with respect to the magnetic field, indicating the antiferromagnetic coupling between the Co and Cr, i.e., the $m_{\text{Cr}}^{\text{U.C.}}$ points down (up) when the magnetization of Co points up (down).

Table 1. Spin magnetic moment (m_{spin}) and orbital magnetic moment (m_{orb}) for the Co, Cr, and N, which are estimated using the Sum rule (see Fig. S6 in Supporting Information).^[57]

Sample	Co	Cr	N	Co (calc) ^{a)}
--------	----	----	---	-------------------------

$[\mu_B/\text{atom}]$	$m_{\text{spin}} / m_{\text{orb}}$	$m_{\text{spin}} / m_{\text{orb}}$	$m_{\text{spin}} / m_{\text{orb}}$	$m_{\text{spin}} / m_{\text{orb}}$
Pure Co	1.83 / 0.17	N.A.	N.A.	1.63 / ~ 0.1
Cr ₂ N / Co	0.99 / 0.73	-0.063 / ~ 0	~ 0 / ~ 0	N.A.
Cr ₂ N / Pt	N.A.	~ 0 / ~ 0	~ 0 / ~ 0	N.A.

a) The values are referred to Ref. [58].

Hereafter, we discuss the possible SOT mechanisms occurred in the Cr₂N/[Co/Pt]₃ system based on a theoretical calculation and control samples. SOT in a ferromagnetic layer generally originates from the spin current generated not only at the bulk part of a spin source layer but also at the interface; therefore, both cases are considered individually. First, the spin diffusion length of pure Cr (λ_s^{Cr}) is reported to be ~ 2.1 nm at RT and ~ 4.5 nm at 4.2 K.^[62,63] Assuming $\lambda_s^{\text{Cr}_2\text{N}} \leq \lambda_s^{\text{Cr}}$, due to the large number of atoms per unit volume in the Cr₂N comparing to the pure Cr,^[62] the ξ_{eff} is considered to decrease in the case of $t_{\text{Cr}_2\text{N}} > \lambda_s^{\text{Cr}_2\text{N}}$, if the spin current would be dominant in the Cr₂N layer. Since the hypothesis cannot be applicable as indicated in Fig. 4(c), it is inferred that the spin current originating from the conventional spin-Hall effect at the bulk part of the Cr₂N layer would be a minor cause, if any. Instead, we must take into account a long-range transport property, which gives rise to the enhanced ξ_{eff} for thicker $t_{\text{Cr}_2\text{N}}$. That is the OHE,^[64] which is generally emerged in the materials consisting of light elements and has longer orbital diffusion length ($\lambda_0^{\text{Cr}} \approx 6.1$ nm) comparing to the λ_s^{Cr} .^[65] The enhanced ξ_{eff} by increasing the Cr thickness in the Co/Cr system has been reported by another group as well, which has been explained by the OHE.^[65,66] In addition to such experimental results, we calculated the spin-Hall conductivity ($\sigma_{xz}^{\text{spin}(k)}$) and orbital-Hall conductivity ($\sigma_{xz}^{\text{orb}(k)}$) in the Cr₂N [Figs. 6(a1) and 6(a2)] to enable the

quantitative comparison between the SHE and OHE contributions in the Cr₂N, where x , z , and k represent the directions of charge current, spin current, and spin/orbital polarization, respectively. Note that we have focused only on the possible spin/orbital current flowing in z -direction that contributes to the CIMS by SOT, but the other components are summarized in Fig. S7 of Supporting Information for more information. Overall, $\sigma_{xz}^{\text{spin}(k)}$ was one or two orders of magnitude smaller than $\sigma_{xz}^{\text{orb}(k)}$, regardless of the k directions. Therefore, the hypothesis of the dominant OHE drawn out from the experiments in Fig. 4(c) can be supported by the theoretical prediction, which is similar to the case of pure Cr: $\sigma^{\text{spin}} \approx -100$ (\hbar/e)(S/cm) and $\sigma^{\text{orb}} \approx 8000$ (\hbar/e)(S/cm).^[67] Furthermore, focusing on the k -dependence of OHE, note that we find $\sigma_{xz}^{\text{orb}(z)} > \sigma_{xz}^{\text{orb}(x)} > \sigma_{xz}^{\text{orb}(y)}$ at the Fermi level as shown in Fig. 6(a2). This means that the orbital current with z -polarization ($k = z$) emerges in the bulk part of Cr₂N in principle, which would be converted into the spin current, and resulting in the out-of-plane SOT for the field-free CIMS. To validate this point, we examined the CIMS properties for the control sample replacing the Cr₂N layer with the Pt layer as shown in Figs. 6(b1)-6(b3). Unlike the results for the Cr₂N/[Co/Pt]₃, the polarity of CIMS was reversed: CW (CCW) for negative (positive) H_x , which might be attributed to the opposite sign of spin/orbital-Hall angle: positive for Pt and negative for Cr₂N. Furthermore, no field-free CIMS was observed, indicating vanishing z -polarized spin current in the Pt layer. This CIMS property is consistent with that observed in the conventional SOT-device such as Pt/CoPt bilayer system, in which y -polarized spin current dominates the CIMS mechanisms.^[56] Then, we decreased the Pt thickness to 1 nm and inserted the 5-nm-thick Cr₂N layer as shown in Figs. 6(c1)-6(c3). As a result, CIMS polarity was maintained as the control sample in Fig. 6(b1), i.e., CW (CCW) for negative (positive) H_x , while the field-free CIMS appeared, though the amplitude of field-free CIMS was still intermediate. These results show the superposition of spin current in the

Pt layer and the z -polarized spin current converted from the pronounced z -polarized orbital current in the bulk part of the Cr_2N layer.

Next, it is essential to consider the interfacial contribution to the out-of-plane SOT, which could dominantly contribute to the field-free CIMS. In the XMCD results, we identified the $m_{\text{Cr}}^{\text{U.C.}}$ oriented in the out-of-plane direction at the interface due to the neighboring Co. Even though the conversion efficiency from orbital to spin might not be strong in the Cr_2N as in the case of pure Cr,^[65] the spin would be scattered or transferred depending on the direction of $m_{\text{Cr}}^{\text{U.C.}}$, which is likely a spin-filtering effect by the $m_{\text{Cr}}^{\text{U.C.}}$ at interface.^[27,42,68] Because of the antiferromagnetic coupling between the $M_{\text{Co/Pt}}$ and the $m_{\text{Cr}}^{\text{U.C.}}$, the polarized spin that is transferred through the interface has always opposite direction to the $M_{\text{Co/Pt}}$, resulting in the field-free deterministic CIMS. As an attempt to boost the spin-filtering-like effect due to $m_{\text{Cr}}^{\text{U.C.}}$, we examined the CIMS property for the control sample with the 1-nm-thick pure Cr insertion as shown in Fig. 6(d1)-6(d3). As a result, the same CIMS polarity and the field-free CIMS were observed as the main sample without 1-nm-thick Cr insertion. Moreover, the amplitude of field-free CIMS was much enhanced comparing to the main sample as plotted in Fig. 2(f), which could be attributed to the enhancement of z -polarized spin component by the $m_{\text{Cr}}^{\text{U.C.}}$ emerged at the $\text{Cr}/[\text{Co/Pt}]_3$ interface. We thus infer that the interfacial spin-filtering-like effect due to $m_{\text{Cr}}^{\text{U.C.}}$ could be a robust and/or universal property for the out-of-plane SOT in addition to the OHE in the bulk mentioned above, which plays one of the crucial roles for the field-free CIMS in the MXene-based SOT-devices.

It should be noted that the noncentrosymmetric materials such as monolayer TMDCs exert out-of-plane SOTs in the adjacent ferromagnetic layer when the direction of charge current flows orthogonal to the mirror plane, in which the sign of out-of-plane SOT reverses with the sign of charge current direction.^[33,34,36] Conversely, the out-of-plane SOT can emerge by the charge

current flowing even in the parallel direction to the mirror plane, which is the specific characteristics for the MXenes that cannot be explained by the conventional scenario with inversion symmetry. In recent years, a mechanism of the OHE that occurs in noncentrosymmetric materials has been examined as an intrinsic property.^[69]

Although various and unknown mechanisms may be considered, the field-free CIMS is more useful in terms of the application of SOT-MRAMs rather than the conventional heavy-metal/ferromagnet system with no field-free CIMS. As the technology node decreases to a few nm by the 2030s, efficient 2D-SOT materials are indispensable in terms of an embedded SOT-MRAM in a CMOS node.^[18] The 2D-MXene has many advantages in principle such as the bottom-up formability by the conventional sputtering, the phase stability up to ~ 650 °C, the sustainable light elements, the process compatibility with CMOS technology. Therefore, 2D-spintronics, represented by SOT-MRAM, would be boosted by MXenes in the future.

Conclusion

One of the 2D-MXenes, Cr₂N, with multilayered structure was developed using the conventional reactive nitridation sputtering process. Judging from the XMCD study, the Cr was polarized by the adjacent ferromagnetic Co, and the $m_{Cr}^{U.C.}$ antiferromagnetically coupled with the magnetic moment of Co. We have successfully demonstrated the CIMS with and without in-plane magnetic field using the sample of substrate//Cr₂N/[Co/Pt]₃/cap. The specific characteristics for the MXene-based SOT-device is the field-free CIMS with critical current density of $\sim 10^7$ A/cm², which is comparable to that for the conventional heavy-metal/ferromagnet system. These results show that new application field of MXene has been opened by expanding into the field of SOT-MRAM that has been unfamiliar. The field-free CIMS can be dominantly attributed to the bulk OHE and the

spin-filtering-like effect at the interface due to $m_{\text{Cr}}^{\text{U.C.}}$, which has not been suggested in the other 2D materials.

METHODS

Film fabrication and characterization

The (0001) plane oriented Al_2O_3 crystal substrate was cleaned with ethanol and acetone by ultrasonic cleaning and flash annealed at 650 °C for 30 min in the sputtering chamber with the base vacuum pressure of $\sim 10^{-7}$ Pa. The Cr_2N film was deposited on the substrate using the DC magnetron reactive sputtering for the Cr target at the T_{sub} from RT to 650 °C with the gas mixture of $\text{N}_2/(\text{Ar} + \text{N}_2) = 5\%$, where the deposition rate was 1.68 nm/min. The Co/Pt multilayer and MgO capping layer were deposited, respectively, using DC and RF magnetron sputtering at RT. The crystal structure was investigated using X-ray diffractometry (SmartLab; Rigaku Corporation) with $\text{Cu-K}\alpha$ radiation and transmission electron microscopy (Titan G2 80-200; Thermo Fisher Scientific Inc. (FEI Company)). The TEM samples for the cross-sectional microstructure was prepared by a focused ion beam lift-out technique (Helios Nanolab 650; Thermo Fisher Scientific Inc. (FEI Company)). To avoid damages on the surface during the milling, the thick Ni film was deposited on top. TEM observation was carried out with a probe aberration corrector. The atomic content was estimated using an energy-dispersive X-ray spectroscopy (EDS) with a Super-X EDX detector (Thermo Fisher Scientific Inc. (FEI Company)). The magnetic properties and anomalous Hall effect were measured at RT using a magnetic property measurement system (MPMS; Quantum Design Inc.) and a physical property measurement system (Dynacool; Quantum Design Inc.), respectively.

Element selective magnetic properties measured via XMCD

The measurements for the XMCD were performed at the BL14U of the synchrotron radiation facility NanoTerasu. Soft X-ray absorption spectra (XAS) were recorded via total electron yield (TEY) method while scanning the photon energy at RT. The XMCD signal was obtained by subtracting each XAS for the circularly polarized light with positive and negative helicities. Especially for Cr and N with tiny magnetic moment, the XAS measurement for each helicity was repeated five times and averaged together to boost signal to noise ratio. The magnetic field was applied in a perpendicular direction to the sample surface. The element selective magnetic properties against the applied field (ESMH) were measured for the L_3 -edge of Co and Cr at RT.

CIMS and second-harmonic measurements

The hand-made system was used for the experiments of CIMS. The current pulse with a rectangular form was applied to the current channel of Hall-cross devices with the duration of ranging from 1 ms to 100 ms using a pulse generator (FG420; Yokogawa Electric Co.). The Hall voltage was recorded using a digital multimeter (7555; Yokogawa Electric Co.) at every interval between current pulses, that is, 1 s after the last current pulse. The DC current for sensing the Hall voltage was 0.5 mA (density: ~ 0.7 MA/cm²), which was applied using a DC power source (G210; Yokogawa Electric Co.). The sensing current density is ~ 2 % of critical current density, which can be negligibly small for CIMS. The magnetic field from an electromagnet was uniform within the gap length of 3 cm and the area size of 5 cm in diameter. Note that the device was put away from the electromagnet for field-free CIMS to eliminate any residual field from the magnetic pole pieces. The second-harmonic Hall voltage was recorded using a lock-in amplifier (LI5640; NF Co.) while scanning the in-plane applied field. The sinusoidal wave with the effective amplitude of 3 mA (density: ~ 4 MA/cm²) and the frequency of 33.123 Hz was applied using a pulse generator (FG420;

Yokogawa Electric Co.). The common device and sample package was used for both CIMS and second-harmonic measurements. All measurements were performed at RT.

Computational procedure for spin/orbital-Hall conductivities

The first-principles calculations were performed by the Vienna ab-initio Simulation Package.^[70] The projector augmented wave (PAW) pseudo-potentials were used for the atomic potentials of Cr and N with the plane-wave cut-off energies 500 eV, respectively.^[71] We adopted the generalized gradient approximation for the exchange and correlation energy including the spin-orbit interaction with $10 \times 10 \times 10$ k-points in the first Brillouin zone.^[72] We considered the on-site Coulomb interaction $U = 3$ eV for Cr atom. Lattice parameters of Cr₂N were the same as Fig. 2(a).^[73] Spin-Hall conductivity (σ^{spin}) and orbital-Hall conductivity (σ^{orb}) are calculated based on the linear response theory as,^[74,75]

$$\sigma_{\alpha\beta}^{\text{X}(\gamma)}(E) = \frac{e}{V} \sum_{\mathbf{k}} \Omega_{\alpha\beta}^{\text{X}(\gamma)}(\mathbf{k}, E). \quad (4)$$

$\Omega_{\alpha\beta}^{\text{X}(\gamma)}(\mathbf{k}, E)$ is the orbital Berry curvature given by,^[75]

$$\Omega_{\alpha\beta}^{\text{X}(\gamma)\gamma}(\mathbf{k}, E) = 2 \frac{\hbar^2}{m_e^2} \sum_{n>m} [f_{\mathbf{k}m}(E) - f_{\mathbf{k}n}(E)] \frac{\text{Im} \langle \mathbf{k}m | (\hat{p}_\alpha^{\text{X}(\gamma)}) | \mathbf{k}n \rangle \langle \mathbf{k}n | \hat{p}_\beta | \mathbf{k}m \rangle}{(\varepsilon_{\mathbf{k}n} - \varepsilon_{\mathbf{k}m})^2}, \quad (5)$$

where V is the volume of the unit-cell, m_e is the electron mass, m and n are the occupied and unoccupied band indices. $\hat{p}_\beta^{\text{X}(\gamma)}$ denotes “spin” or “orbital” current operator ($X=\text{spin}$ or orbital), where $\hat{p}_\alpha^{\text{spin}(\gamma)} = \hat{p}_\alpha \hat{s}_\gamma + \hat{s}_\gamma \hat{p}_\alpha$ and $\hat{p}_\alpha^{\text{orbital}(\gamma)} = \hat{p}_\alpha \hat{L}_\gamma + L_\gamma \hat{p}_\alpha \cdot \hat{p}_\alpha$ (\hat{p}_β) is the α (β)-axis component of the momentum operator, \hat{s}_γ is the spin angular momentum operator with the spin

quantum axis along γ direction, and \hat{L}_γ is the orbital angular momentum operator along γ direction. $|\mathbf{k}n\rangle$ is the eigenstate with the eigenenergy $\varepsilon_{\mathbf{k}n}$, and $f_{\mathbf{k}n}(E)$ is the occupation function for the band n and wave-vector \mathbf{k} at the energy (E) relative to the Fermi level (E_F). The $\sigma^{\text{spin(orb)}}$ of Cr_2N was computed using $30 \times 30 \times 30$ k-points in the first Brillouin zone.

FIGURES

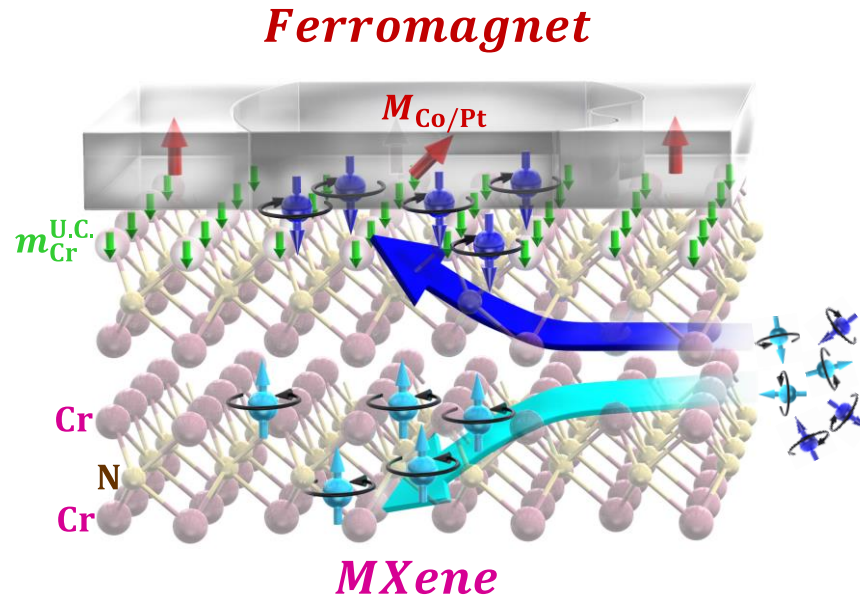


Figure 1. Concept of the field-free CIMS in the two-dimensional MXene-based SOT-device, i.e., the MXene (Cr_2N)/ferromagnet bilayer system. The electron-spins oriented in the out-of-plane direction emerge through the pronounced orbital-Hall effect in the MXene layer. The thick green arrows at the interface represent the out-of-plane uncompensated magnetic moment of Cr ($m_{\text{Cr}}^{\text{U.C.}}$) induced by the adjacent ferromagnetic layer. The $m_{\text{Cr}}^{\text{U.C.}}$ can act as a spin-filter that transfers the polarized electron-spins with the same orientation as the $m_{\text{Cr}}^{\text{U.C.}}$. The out-of-plane oriented spins exert the torque on the ferromagnetic layer, resulting in the magnetic domain switching without in-plane magnetic fields.

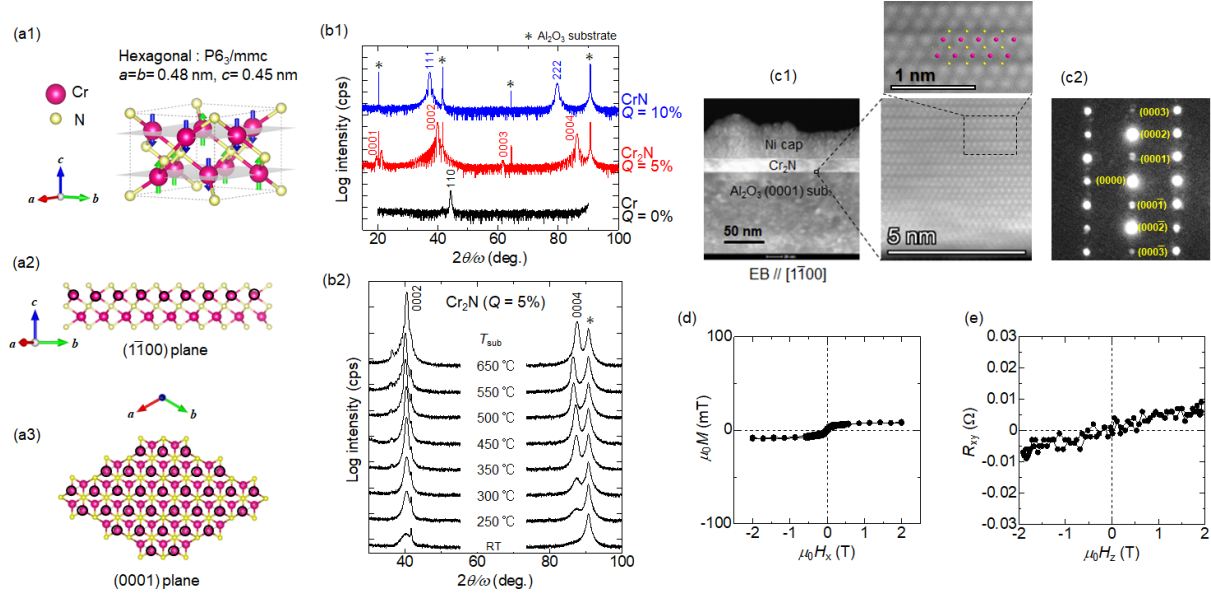


Figure 2. (a1) Unit cell model of the Cr_2N bare MXene together with the possible magnetic structure predicted by first-principles calculation. (a2, a3) Cross-sectional view (a2) and plane view (a3) for the $3 \times 3 \times 1$ supercell, where the Cr atoms at the top layer are surrounded by black circles. (b1, b2) Out-of-plane XRD profiles for the 20-nm-thick Cr-N films deposited with different N_2 flow ratio $Q = \text{N}_2/(\text{Ar}+\text{N}_2)$ while reactive sputtering deposition (b1), and substrate temperature (T_{sub}) (b2). (c1, c2) Cross-sectional TEM images (c1) and nano electron-beam diffraction (NBD) pattern (c2) with the electron beam incidence along $[1\bar{1}00]$ direction. In the magnified high-resolution TEM image, Cr atom is seen in bright color. In the NBD pattern, the large bright and the small dark spots correspond to the diffractions from the fundamental lattice and superlattice planes, respectively. (d) Magnetization curve measured by the in-plane magnetic field (H_x). (e) Anomalous Hall resistance as a function of out-of-plane magnetic field (H_z).

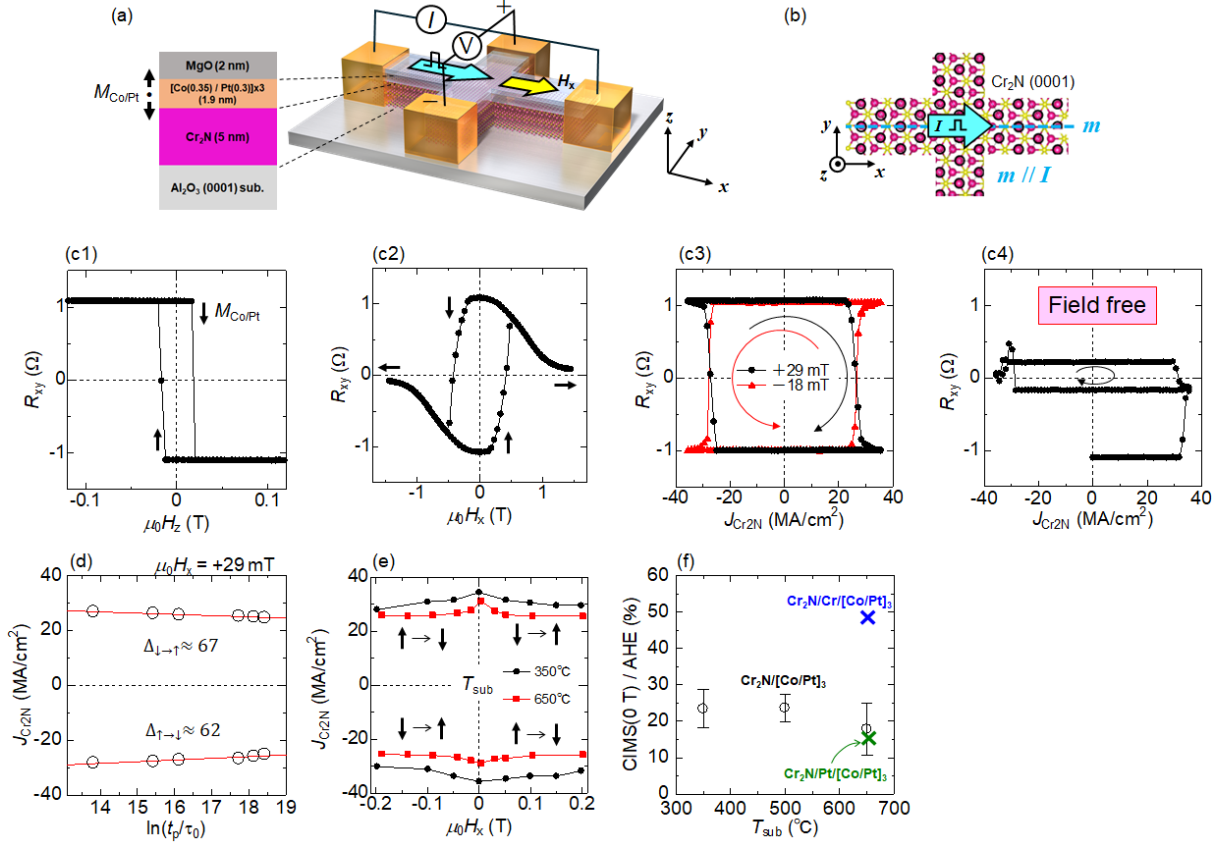


Figure 3. (a) Measurement configuration of the current-induced magnetization switching (CIMS) and representative stacking structure, where the 5-nm-thick MXene layer consists of ~ 10 unit-layer of Cr_2N . (b) Direction of the current pulse for the CIMS demonstration. (c1-c4) Anomalous Hall resistance for the same sample with the magnetic field along the out-of-plane (H_z) (c1) and in-plane (H_x) (c2) directions. Representative CIMS under the bias field of $\mu_0 H_x = +29$ mT, -18 mT (c3), and 0 (field free) (c4). (d) Critical current density of the Cr_2N layer ($J_{\text{Cr}_2\text{N}}$) as a function of pulse duration (t_p) ranging from 1 ms to 100 ms. The red line represents the fitting result using Eq. (1) to evaluate the thermal stability factor (Δ). (e) H_x dependence of $J_{\text{Cr}_2\text{N}}$ for the Cr_2N growth temperature (T_{sub}) of 350 °C and 650 °C. (f) Partial field-free CIMS ratio relative to the full switching by H_z [Fig. 3(c1)] for various T_{sub} . The green and blue symbols represent the same results, but with the insertion of 1-nm-thick Cr and Pt layers, respectively, for comparison.

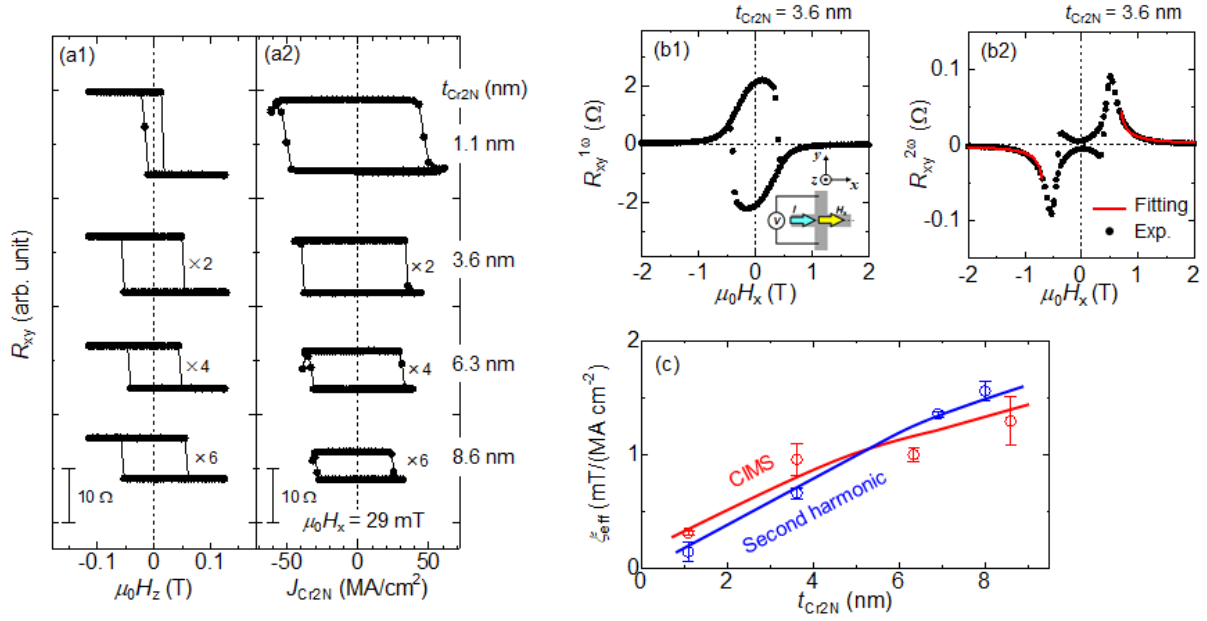


Figure 4. (a1, a2) Cr₂N layer thickness (t_{Cr2N}) dependence of the out-of-plane AHE (a1) and CIMS loops (a2) with the bias field $\mu_0 H_x = +29$ mT, for the SOT-device of substrate//Cr₂N(t_{Cr2N})/[Co(0.35 nm)/Pt(0.3 nm)]₃/MgO(2 nm). (b1, b2) High-field in-plane AHE loops for the first-harmonic (1ω) (b1) and second-harmonic (2ω) (b2) Hall resistance. The red curve in Fig. 4(b2) represents the fitting result using Eq. (2) to distinguish the damping-like (H_{DL}) and field-like (H_{FL}) SOT effective fields from the magneto thermoelectric effect. (c) Damping-like SOT efficiency (ξ_{eff}) as a function of t_{Cr2N} estimated by both the critical J_{Cr2N} in CIMS loops (red) and the H_{DL} value in the second-harmonic measurements (blue).

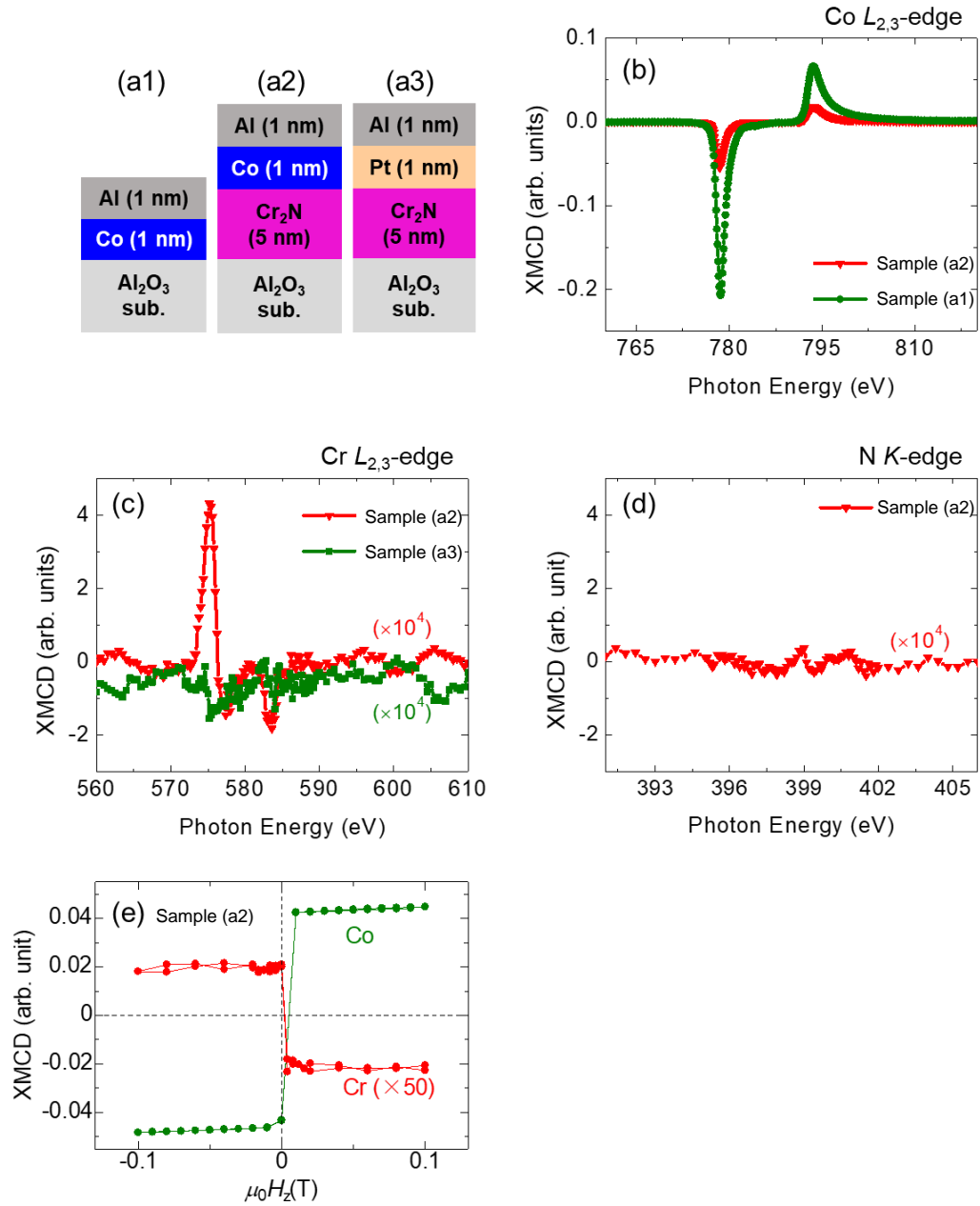


Figure 5. (a1-a3) Stacking structures for the XMCD measurement at the synchrotron radiation facility. (b-d) XMCD spectra for the Co $L_{2,3}$ -edge (b), Cr $L_{2,3}$ -edge (c), and N K -edge (d) of the samples shown in Fig. 5(a1-a3). (e) Element-selective out-of-plane magnetic properties for Co and Cr of the sample (a2).

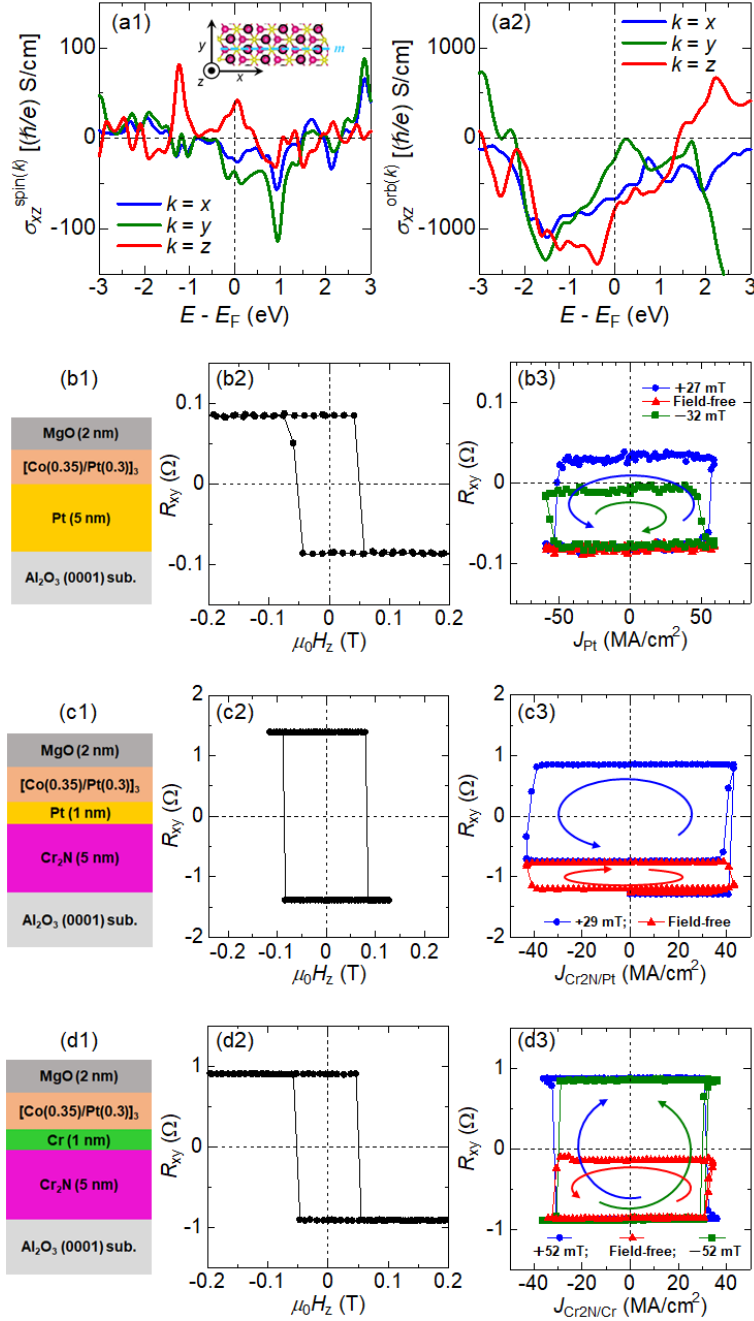


Figure 6. (a) Energy dependent spin-Hall conductivity ($\sigma_{xz}^{\text{spin}(k)}$) and orbital-Hall conductivity ($\sigma_{xz}^{\text{orb}(k)}$) for the Cr_2N , where x , z , and k represent the directions of charge current, spin current, and spin/orbital polarization, respectively. (b-d) CIMS results for the control samples, replacing the Cr_2N layer with the Pt layer (b), with 1-nm-thick Pt layer insertion (c), and with 1-nm-thick Cr insertion (d), respectively.

REFERENCES

- [1] A. K. Geim, S. V. Morozov, D. Jiang, Y. Zhang, S. V. Dubonos, I. V. Grigorieva, A. A. Firsov and K. S. Novoselov. Electric Field Effect in Atomically Thin Carbon Films. *Science* **2004**, 306, 666.
- [2] Q. H. Wang, K. K.-Zadeh, A. Kis, J. N. Coleman, and M. S. Strano. Electronics and optoelectronics of two-dimensional transition metal dichalcogenides. *Nature Nanotech.* **2012**, 7, 699.
- [3] B. Radisavljevic, A. Radenovic, J. Brivio, V. Giacometti, and A. Kis. Single-layer MoS₂ transistors. *Nature Nanotech.* **2011**, 6, 147.
- [4] H. Fang, S. Chuang, T. C. Chang, K. Takei, T. Takahashi, and A. Javey. High-Performance Single Layered WSe₂ p-FETs with Chemically Doped Contacts. *Nano Lett.* **2012**, 12, 3788.
- [5] B. Radisavljevic, M. B. Whitwick, and A. Kis. Integrated Circuits and Logic Operations Based on Single-Layer MoS₂. *ACS Nano.* **2011**, 12, 9934.
- [6] A. Pospischil, M. M. Furchi, and T. Mueller. Solar-energy conversion and light emission in an atomic monolayer p–n diode. *Nature Nanotech.* **2014**, 9, 257.
- [7] A. Splendiani, L. Sun, Y. Zhang, T. Li, J. Kim, C.-Y. Chim, G. Galli, and F. Wang. Emerging Photoluminescence in Monolayer MoS₂. *Nano Lett.* **2010**, 10, 1271.
- [8] Y. Cao, V. Fatemi, S. Fang, K. Watanabe, T. Taniguchi, E. Kaxiras, and P. J.-Herrero. Unconventional superconductivity in magic-angle graphene superlattices. *Nature* **2017**, 556, 43.
- [9] Y. Qi, M. A. Sadi, D. Hu, M. Zheng, Z. Wu, Y. Jiang, and Y. P. Chen. Recent Progress in Strain Engineering on Van der Waals 2D Materials: Tunable Electrical, Electrochemical, Magnetic, and Optical Properties. *Adv. Mater.* **2023**, 35, 2205714.
- [10] M. Naguib, M. Kurtoglu, V. Presser, J. Lu, J. Niu, M. Heon, L. Hultman, Y. Gogotsi, and M. W. Barsoum. Two-Dimensional Nanocrystals Produced by Exfoliation of Ti₃AlC₂. *Adv. Mater.* **2011**, 23, 4248.

- [11] M Naguib, V. N. Mochalin, M. W. Barsoum, and Y. Gogotsi. Two-Dimensional Materials: 25th Anniversary Article: MXenes: A New Family of Two-Dimensional Materials. *Adv. Mater.* **2014**, 26, 992.
- [12] X. Li, M. Li, Z. Huang, G. Liang, Z. Chen, Q. Yang, Q. Huang, and C. Zhi. Activating the I^0/I^+ redox couple in an aqueous I_2 -Zn battery to achieve a high voltage plateau. *Energy Environ. Sci.* **2021**, 14, 407.
- [13] S. Isogami, and Y. K. Takahashi. Antiperovskite Magnetic Materials with 2p Light Elements for Future Practical Applications. *Adv. Electron. Mater.* **2023**, 9, 2200515.
- [14] N. Driscoll, A. G. Richardson, K. Maleski, B. Anasori, O. Adewole, P. Lelyukh, L. Escobedo, D. K. Cullen, T. H. Lucas, Y. Gogotsi, and F. Vitale. Two-Dimensional Ti_3C_2 MXene for High-Resolution Neural Interfaces. *ACS Nano* **2018**, 12, 10419.
- [15] J. Zhang, N. Kong, S. Uzun, A. Levitt, S. Seyedin, P. A. Lynch, S. Qin, M. Han, W. Yang, J. Liu, X. Wang, Y. Gogotsi, and J. M. Razal. Scalable Manufacturing of Free-Standing, Strong $Ti_3C_2T_x$ MXene Films with Outstanding Conductivity. *Adv. Mater.* **2020**, 32, 2001093.
- [16] S. Ahn, T.-H. Han, K. Maleski, J. Song, Y.-H. Kim, M.-H. Park, H. Zhou, S. Yoo, Y. Gogotsi, and T.-W. Lee. A 2D Titanium Carbide MXene Flexible Electrode for High-Efficiency Light-Emitting Diodes. *Adv. Mater.* **2020**, 32, 2000919.
- [17] S. Zhao, X. Meng, K. Zhu, F. Du, G. Chen, Y. Wei, Y. Gogotsi, and Y. Gao. Li-ion uptake and increase in interlayer spacing of Nb_4C_3 MXene. *Energy Storage Materials* **2017**, 8, 42.
- [18] H. Yang, S. O. Valenzuela, M. Chshiev, S. Couet, B. Dieny, B. Dlubak, A. Fert, K. Garello, M. Jamet, D.-E. Jeong, K. Lee, T. Lee, M.-B. Martin, G. S. Kar, P. Sénéor, H.-J. Shin, and S. Roche. Two-dimensional materials prospects for non-volatile spintronic memories. *Nature* **2022**, 606, 663.
- [19] Y. Liu and Q. Shao. Two-Dimensional Materials for Energy Efficient Spin-Orbit Torque Devices. *ACS Nano* **2020**, 14, 9389.
- [20] S. Maekawa, T. Kikkawa, H. Chudo, J. Ieda, E. Saitoh. Spin and spin current—From fundamentals to recent progress. *J. Appl. Phys.* **2023**, 133, 020902.

- [21] V. D. Nguyen , S. Rao, K. Wostyn, and S. Couet. Recent progress in spin-orbit torque magnetic random-access memory. *npj Spintronics* **2024**, 2, 48.
- [22] S. Fukami, T. Anekawa, C. Zhang, and H. Ohno. A spin–orbit torque switching scheme with collinear magnetic easy axis and current configuration. *Nature Nanotech.* **2016**, 11, 621.
- [23] H. Wu, J. Zhang, B. Cui, S. A. Razavi, X. Che, Q. Pan, D. Wu, G. Yu, X. Han, and K. L. Wang. Field-free approaches for deterministic spin–orbit torque switching of the perpendicular magnet. *Mater. Futures* **2022**, 1, 022201.
- [24] T.-Y. Chen, H.-I Chan, W.-B. Liao, and C.-F. Pai. Current-Induced Spin-Orbit Torque and Field-Free Switching in Mo-Based Magnetic Heterostructures. *Phsy. Rev. Appl.* **2018**, 10, 044038.
- [25] Z. Zheng, Y. Zhang, V. L.-Dominguez, L. S.-Tejerina, J. Shi, X. Feng, L. Chen, Z. Wang, Z. Zhang, K. Zhang, B. Hong, Y. Xu, Y. Zhang, M. Carpentieri, A. Fert, G. Finocchio, W. Zhao, and P. K. Amiri. Field-free spin-orbit torque-induced switching of perpendicular magnetization in a ferrimagnetic layer with a vertical composition gradient. *Nature Communications* **2021**, 12, 4555.
- [26] V. P. Amin, J. Zemen, and M. D. Stiles. Interface-Generated Spin Currents. *Phys. Rev. Lett.* **121**, 136805 (2018).
- [27] G. Choi, J. Ryu, S. Lee, J. Kang, N. Noh, J. M. Yuk, B.-G. Park. Thickness Dependence of Interface-Generated Spin Currents in Ferromagnet/Ti/CoFeB Trilayers. *Adv. Mater. Int.* **2022**, 9, 2201317.
- [28] S. Fukami, C. Zhang, S. DuttaGupta, A. Kurenkov, and H. Ohno. Magnetization switching by spin–orbit torque in an antiferromagnet–ferromagnet bilayer system. *Nature Mater.* **2016**, 15, 535.
- [29] Y.-C. Lau, D. Betto, K. Rode, J. M. D. Coey, and P. Stamenov. Spin–orbit torque switching without an external field using interlayer exchange coupling. *Nature Nanotech.* **2016**, 11, 758.

- [30] Y. You, H. Bai, X. Feng, X. Fan, L. Han, X. Zhou, Y. Zhou, R. Zhang, T. Chen, F. Pan, and C. Song. Cluster magnetic octupole induced out-of-plane spin polarization in antiperovskite antiferromagnet. *Nature Communications* **2021**, 12, 6524.
- [31] S. Hu, D.-F. Shao, H. Yang, C. Pan, Z. Fu, M. Tang, Y. Yang, W. Fan, S. Zhou, E. Y. Tsymbal, and X. Qiu. Efficient perpendicular magnetization switching by a magnetic spin Hall effect in a noncollinear antiferromagnet. *Nature Communications* **2022**, 13, 4447.
- [32] C. Cao, S. Chen, R.-C. Xiao, Z. Zhu, G. Yu, Y. Wang, X. Qiu, L. Liu, T. Zhao, D.-F. Shao, Y. Xu, J. Chen, and Q. Zhan. Anomalous spin current anisotropy in a noncollinear antiferromagnet. *Nature Communications* **2023**, 14, 5873.
- [33] D. Macneill, G. M. Stiehl, M. H. D. Guimaraes, R. A. Buhrman, J. Park, D. C. Ralph. Control of spin-orbit torques through crystal symmetry in WTe₂/ferromagnet bilayers. *Nat. Phys.* **2017**, 13, 300.
- [34] I.-H. Kao, R. Muzzio, H. Zhang, M. Zhu, J. Gobbo, S. Yuan, D. Weber, R. Rao, J. Li, J. H. Edgar, J. E. Goldberger, J. Yan, D. G. Mandrus, J. Hwang, R. Cheng, J. Katoch, and S. Singh. Deterministic switching of a perpendicularly polarized magnet using unconventional spin-orbit torques in WTe₂. *Nature Materials* **2022**, 21, 1029.
- [35] S. N. Kajale, T. Nguyen, N. T. Hung, M. Li, D. Sarkar. Field-free deterministic switching of all-van der Waals spin-orbit torque system above room temperature. *Sci. Adv.* **2024**, 10, 8669.
- [36] X. Wang, H. Wu, R. Qiu, X. Huang, J. Zhang, J. Long, Y. Yao, Y. Zhao, Z. Zhu, J. Wang, S. Shi, H. Chang, W. Zhao. Room temperature field-free switching of CoFeB/MgO heterostructure based on large-scale few-layer WTe₂. *Cell Rep. Phys. Sci.* **2023**, 4, 101468.
- [37] I. Shin, W. J. Cho, E.-S. An, S. Park, H.-W. Jeong, S. Jang, W. J. Baek, S. Y. Park, D.-H. Yang, J. H. Seo, G.-Y. Kim, M. N. Ali, S.-Y. Choi, H.-W. Lee, J. S. Kim, S. D. Kim, and G.-H. Lee. Spin-Orbit Torque Switching in an All-Van der Waals Heterostructure. *Adv. Mater.* **2022**, 34, 2101730.
- [38] E. Grimaldi, V. Krizakova, G. Sala, F. Yasin, S. Couet, G. S. Kar, K. Garello, and P. Gambardella. Single-shot dynamics of spin-orbit torque and spin transfer torque switching in three-terminal magnetic tunnel junctions. *Nature Nanotech.* **2020**, 15, 111.

- [39] N. Sato, 2020 Symposia on VLSI Technology and Circuits, Honolulu (Virtual), June **2020**.
- [40] S. Khan, A. Mahmood, A. Shah, Q. Raza, M. A. Rasheed, and I. Ahmad. Structural and optical analysis of Cr₂N thin films prepared by DC magnetron sputtering. *Int. J. Miner. Metall. Mater.* **2015**, 22, 197.
- [41] M. A. Gharavi, G. Greczynski, F. Eriksson, J. Lu, B. Balke, D. Fournier, A. le Febvrier, C. Pallier, and P. Eklund. Synthesis and characterization of single-phase epitaxial Cr₂N thin films by reactive magnetron sputtering. *J. Mater. Sci.* **2019**, 54, 1434.
- [42] T. Song, X. Cai, M. W.-Y. Tu, X. Zhang, B. Huang, N. P. Wilson, K. L. Seyler, L. Zhu, T. Taniguchi, K. Watanabe, M. A. McGuire, D. H. Cobden, D. Xiao, W. Yao, X. Xu. Giant tunneling magnetoresistance in spin-filter van der Waals heterostructures. *Science* **2018**, 360, 1214.
- [43] J. D. Browne, P. R. Liddell, R. Street, and T. Mills. An Investigation of the Antiferromagnetic Transition of CrN. *Phys. Stat. Sol. (a)* **1970**, 1, 715.
- [44] G. Wang. Theoretical Prediction of the Intrinsic Half-Metallicity in Surface Oxygen-Passivated Cr₂N MXene. *J. Phys. Chem. C* **2016**, 120, 18850.
- [45] H. Kumar, N. C. Frey, L. Dong, and V. B. Shenoy. Tunable Magnetism and Transport Properties in Nitride MXenes. *ACS Nano* **2017**, 11, 7648.
- [46] S. J. G.-Ojeda, R. P.-Pérez, D. M.-Lopez, D. M. Hoat, J. G.-Sánchez, M. G. M.-Armenta. Strain Effects on the Two-Dimensional Cr₂N MXene: An Ab Initio Study. *ACS Omega* **2022**, 7, 33884.
- [47] S. J. G.-Ojeda, R. P.-Pérez, J. G.-Sánchez, M. G. M.-Armenta. MXene heterostructures based on Cr₂C and Cr₂N: evidence of strong interfacial interactions that induce an antiferromagnetic alignment. *Graphene and 2D Materials* **2024**, 9, 47.
- [48] S. Isogami, Y. Shiokawa, A. Tsumita, E. Komura, Y. Ishitani, K. Hamanaka, T. Taniguchi, S. Mitani, T. Sasaki, and M. Hayashi. Spin-orbit torque driven magnetization switching in W/CoFeB/MgO-based type-Y three terminal magnetic tunnel junctions. *Sci. Rep.* **2022**, 11, 16676.

- [49] D. Bedau, H. Liu, J. Z. Sun, J. A. Katine, E. E. Fullerton, S. Mangin, and A. D. Kent. Spin-transfer pulse switching: From the dynamic to the thermally activated regime. *Appl. Phys. Lett.* **2010**, 97, 262502.
- [50] T. Taniguchi, S. Isogami, Y. Shiokawa, Y. Ishitani, E. Komura, T. Sasaki, S. Mitani, and M. Hayashi. Magnetization switching probability in the dynamical switching regime driven by spin-transfer torque. *Phys. Rev. B* **2022**, 106, 104431.
- [51] G. J. Lim, W. L. Gan, W. C. Law, C. Murapaka, W. S. Lew. Spin-orbit torque induced multi-state magnetization switching in Co/Pt hall cross structures at elevated temperatures. *J. Magn. Magn. Mater.* **2020**, 514, 167201.
- [52] S. Ishikawa, H. Sato, M. Yamanouchi, S. Ikeda, S. Fukami, F. Matsukura, and H. Ohno. Co/Pt multilayer-based magnetic tunnel junctions with a CoFeB/Ta insertion layer. *J. Appl. Phys.* **2014**, 115, 17C719.
- [53] B. Jinnai, C. Zhang, A. Kurenkov, M. Bersweiler, H. Sato, S. Fukami, and H. Ohno. Spin-orbit torque induced magnetization switching in Co/Pt multilayers. *Appl. Phys. Lett.* **2017**, 111, 102402.
- [54] O. J. Lee, L. Q. Liu, C. F. Pai, Y. Li, H. W. Tseng, P. G. Gowtham, J. P. Park, D. C. Ralph, and R. A. Buhrman. Central role of domain wall depinning for perpendicular magnetization switching driven by spin torque from the spin Hall effect. *Phys. Rev. B* **2014**, 89, 024418.
- [55] X. Qiu, W. Legrand, P. He, Y. Wu, J. Yu, R. Ramaswamy, A. Manchon, and H. Yang. Enhanced Spin-Orbit Torque via Modulation of Spin Current Absorption. *Phys. Rev. Lett.* **2016**, 117, 217206.
- [56] C. O. Avci, K. Garello, M. Gabureac, A. Ghosh, A. Fuhrer, S. F. Alvarado, and P. Gambardella. Interplay of spin-orbit torque and thermoelectric effects in ferromagnet/normal-metal bilayers. *Phys. Rev. B* **2014**, 90, 224427.
- [57] B. T. Thole, P. Carra, F. Sette, and G. van der Laan. X-ray circular dichroism as a probe of orbital magnetization. *Phys. Rev. Lett.* **1992**, 68, 1943.

- [58] P. Carra, B.T. Thole, M. Altarelli, and X. Wang. X-Ray Circular Dichroism and Local Magnetic Fields. *Phys. Rev. B* **1993**, 70, 694.
- [59] O. Hjortstam, J. Trygg, J. M. Wills, B. Johansson, and O. Eriksson. Calculated spin and orbital moments in the surfaces of the 3d metals Fe, Co, and Ni and their overlayers on Cu(001). *Phys. Rev. B* **1996**, 53, 9204.
- [60] Y. Shiratsuchi, H. Noutomi, H. Oikawa, T. Nakamura, M. Suzuki, T. Fujita, K. Arakawa, Y. Takechi, H. Mori, T. Kinoshita, M. Yamamoto, and R. Nakatani. Detection and In Situ Switching of Unreversed Interfacial Antiferromagnetic Spins in a Perpendicular-Exchange-Biased System. *Phys. Rev. Lett.* **2012**, 109, 077202.
- [61] C. S.-Hanke, R. G.-Arrabal, J. E. Prieto, E. Andrzejewska, N. Gordillo, D. O. Boerma, R. Loloee, J. Skuza, R. A. Lukaszew. Observation of nitrogen polarization in Fe-N using soft x-ray magnetic circular dichroism. *J. Appl. Phys.* **2006**, 99, 08B709.
- [62] J. Bass, W. P Pratt Jr. Spin-diffusion lengths in metals and alloys, and spin-flipping at metal/metal interfaces: an experimentalist's critical review. *J. Phys.: Condens. Matter.* **2007**, 19, 183201.
- [63] D. Qu, S. Y. Huang, and C. L. Chien. Inverse spin Hall effect in Cr: Independence of antiferromagnetic ordering. *Phys. Rev. B* **2015**, 92, 020418(R).
- [64] B. A. Bernevig, T. L. Hughes, and S.-C. Zhang. Orbitronics : The Intrinsic Orbital Current in p-Doped Silicon. *Phys. Rev. Lett.* **2005**, 95, 066601.
- [65] S. Lee, M.-G. Kang, D. Go, D. Kim, J.-H. Kang, T. Lee, G.-H. Lee, J. Kang, N. J. Lee, Y. Mokrousov, S. Kim, K.-J. Lee, B.-G. Park. Efficient conversion of orbital Hall current to spin current for spin-orbit torque switching. *Comm. Phys.* **2021**, 4, 234.
- [66] G. Sala, and P. Gambardella. Giant orbital Hall effect and orbital-to-spin conversion in 3d, 5d, and 4f metallic heterostructures. *Phys. Rev. Res.* **2022**, 4, 033037.
- [67] D. Jo, D. Go, and H.-W. Lee. Gigantic intrinsic orbital Hall effects in weakly spin-orbit coupled metals. *Phys. Rev. B* **2018**, 98, 214405.

- [68] V. P. Amin, P. M. Haney, and M. D. Stiles. Interfacial spin–orbit torques. *J. Appl. Phys.* **2020**, 128, 151101.
- [69] S. Bhowal, and S. Satpathy. Intrinsic orbital moment and prediction of a large orbital Hall effect in two-dimensional transition metal dichalcogenides. *Phys. Rev. B* **2020**, 101, 121112(R).
- [70] G. Kresse and J. Furthmüller. Efficient iterative schemes for ab initio total-energy calculations using a plane-wave basis set. *Phys. Rev. B* **1996**, 54, 11169.
- [71] P. E. Blöchl. Projector augmented-wave method. *Phys. Rev. B* **1994**, 50, 17953.
- [72] J. P. Perdew, K. Burke, and M. Ernzerhof. Generalized gradient approximation made simple. *Phys. Rev. Lett.* **1996**, 77, 3865.
- [73] V. I. Anisimov, J. Zaanen, and O. K. Andersen. Band theory and Mott insulators: Hubbard U instead of Stoner I. *Phys. Rev. B* **1991**, 44, 943.
- [74] H. Nakano. A method of calculation of electrical conductivity. *Prog. Theor. Phys.* **1956**, 15, 77.
- [75] R. Kubo. Statistical mechanical theory of irreversible processes: General theory and simple applications in magnetic and conduction problems. *J. Phys. Soc. Jpn.* **1957**, 12, 570.
- [76] Y. Miura, and K. Masuda. First-principles calculations on the spin anomalous Hall effect of ferromagnetic alloys. *Phys. Rev. Mater.* **2021**, 5, L101402.